energies

Article

A Feasibility Study on the Lateral Behavior of a 3D-Printed Column for Application in a Wind Turbine Tower

In-Hwan Yang [1,*], Quang-The Bui [1], Ji-Hun Park [2] and Seung-Tae Jeong [1]

[1] Department of Civil Engineering, Kunsan National University, Kunsan 54150, Republic of Korea
[2] Department of Structural Engineering Research, Korea Institute of Civil Engineering and Building Technology, Goyang 10223, Republic of Korea
* Correspondence: ihyang@kunsan.ac.kr

Abstract: Although 3D printing technology has been applied worldwide, the problem of connecting a printed structure and a foundation has rarely been examined. In particular, loads in the horizontal direction, such as wind loads and earthquake loads, can significantly affect the stability of a printed structure. Therefore, in this study, the effect of lateral loads on printed columns that were connected to a foundation by two types of connectors was investigated. A steel angle with bolts and couplers was used to connect the printed column to a concrete footing. In addition, two types of lateral reinforcement were applied to the printed column to enhance its bonding strength and shear resistance. The lateral reinforcements were attached to the interface of the printed layers at distances of 100 and 200 mm to investigate the effect of lateral reinforcement distance on the lateral behavior of the printed column. The results showed that the use of couplers as connections between the columns and foundation significantly improved the load capacity. Furthermore, the effects of the lateral reinforcement types and lateral reinforcement distances were assessed.

Keywords: 3D concrete; connection; lateral behavior; wind turbine tower; printed structure

Citation: Yang, I.-H.; Bui, Q.-T.; Park, J.-H.; Jeong, S.-T. A Feasibility Study on the Lateral Behavior of a 3D-Printed Column for Application in a Wind Turbine Tower. *Energies* **2023**, *16*, 7218. https://doi.org/10.3390/en16207218

Academic Editors: Andrzej Pacana and Dominika Siwiec

Received: 6 September 2023
Revised: 16 October 2023
Accepted: 20 October 2023
Published: 23 October 2023

1. Introduction

Additive manufacturing techniques have gained increasing attention in the construction industry, and their application has become more common and commercialized [1–3]. In 2014, ten basic houses were printed by the Chinese Winsun Company in just one day [4]. In 2015, this company built a five-story apartment building with an area of approximately 1100 m^2, which is currently the tallest 3D-printed structure. The Apis Cor Company is known as the first company in the USA to apply 3D printing technology in construction [5]. In 2016, a Chinese company, Huashang Tengda, announced that a two-story onsite building was printed within 45 days by using a unique process [6]. Because the printed building was enhanced by rebar, the company assured that this printed structure was durable enough to withstand an earthquake measuring 8.0 on the Richter scale. In 2017, a 3D-printed concrete pedestrian bridge was opened to the public and designed by a department of the Built Environment, the Eindhoven University of Technology in The Netherlands [7]. Before operation, this prestressed bridge was tested onsite to ensure its safety. The application of 3D printing technology was realized by the US Army when used to print a barracks [8] in 2017. In this project, two structures were printed and distinguished by the wall shape and the connection type with the foundation. A cost comparison indicated that the 3D printing method not only reduced the construction time but also lowered the cost of the structure. Recently, in 2019, a team from Tsinghua University School of Architecture built the world's longest 3D-printed concrete bridge with a length of approximately 26 m in Shanghai [9]. This printed bridge was produced over 450 h and incurred a third of the costs of a comparable traditional bridge.

The 3D printing of concrete, also known as the additive manufacturing of concrete, involves depositing layers of concrete material in a precise and controlled manner to build up a 3D structure. This process is typically achieved using a large-scale 3D printer that can accommodate the size and weight of the printed object. In the case of wind turbine towers, 3D printing offers several advantages over traditional methods. For example, a 3D-printed foundation can be designed with greater precision and optimization, accounting for factors such as soil conditions, wind loads, and seismic activity. This control can result in a more efficient use of materials and reduced construction time. Recently, the feasibility of 3D printing concrete in wind turbine tower construction has been evaluated [10]. It was reported that fabricating a wind turbine tower with 3D-printed concrete reduced CO_2 emissions by 23% compared to a steel tower. Moreover, 3D printing can reduce the need for the manual labor and equipment typically needed for traditional concrete construction, as the printing process can be largely automated. In addition, it has been indicated that logistical complexity and expense are significant when moving large tower components to their designated installation locations. To address this problem, GE Renewable Energy, Cobod, and Lafarge Holcim cooperated to print the first wind turbines with optimized 3D-printed concrete bases in the world [11], as shown in Figure 1. The 3D-printed concrete bases, with heights up to 200 m, were expected to optimize construction costs and reduce execution times. Wind turbine towers have conventionally been constructed using steel or precast concrete, with a usual height constraint of less than 100 m. This limitation arises from the necessity to keep the base width within a diameter of 4.5 m, a size transportable by road without incurring substantial extra expenses. To better understand the real application of 3D-printed wind turbine towers in the industrial world, it is necessary to investigate their structural behaviors, such as under static loads, seismic loads, and blast loads. However, few of these investigations have been carried out.

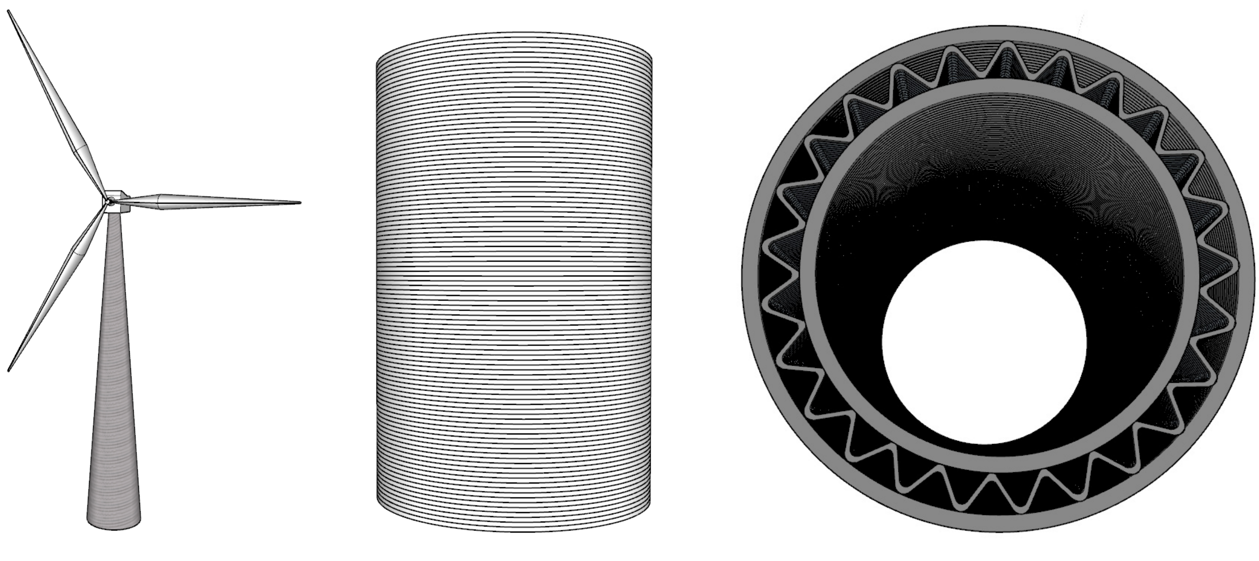

(**a**) (**b**) (**c**)

Figure 1. Sky-High wind tower printed by 3D technique [11]. (**a**) Modeling of Sky-High wind tower; (**b**) side view; (**c**) top view.

Although the 3D printing technique has been widely applied, a method to connect printed structures and foundations has rarely been the focus of previous studies. Most of the printed structures were laminated as masonry with double walls and laid on even footings. Then, the joint between the masonry and foundation is filled with grout. Using this process, the printed structures can be temporally fitted to the footing, but it is considered that the structures are weak under lateral loads. In addition, the printed structure and foundation can be connected using the existing rebar fabricated with the footing [12,13]. While this connecting method can seemingly combine the structure and foundation, the existing rebars can preclude the use of a printing process, or a particular nozzle may be needed. A discontinuous printing process can affect the designed shape of the structure or generate cold joints at the interface of the printed layers [14]. In addition, preinstalled reinforcement for the printed structure limits the geometric freedom of 3D printing [15].

Numerous studies have been carried out to enhance the bonding strength of 3D-printed concrete [16–18]. Hass and Bos [19] presented a novel reinforcement method utilizing screw-type reinforcements, which showed improved interlayer bonding strength in printed concrete according to the failure patterns observed in 3-point bending and pull-out tests. Park et al. [20] investigated the effect of the overlap length of screwed interlayer reinforcement on the bonding strength of 3D concrete. It was reported that the longer overlap length of the interlayer reinforcement significantly improved the postcracking behavior of 3D-printed concrete. Another reinforcement method was introduced by Ma et al. [21] involving microcables, which led to improved flexural strength and postcracking softening behavior in printed concrete. Similarly, the addition of straight steel fibers into mortar filaments was reported to enhance the ductile postcracking behavior of printed mortar, as observed in a study conducted by Bester et al. [22]. Perrot et al. [23] found that the addition of nails to concrete layers enhanced the flexural tensile strength and ductility of printed specimens. Bos et al. [24] concluded that the precracking and postcracking strength of 3D-printed specimens significantly improved with the addition of cable reinforcements.

Therefore, based on the limitations of previous studies, this study was carried out to investigate the characteristics of a novel connecting method between a 3D-printed structure and foundation. The lateral behavior of columns with two different connections was also examined. In addition, to improve the bonding strength and shear resistance, different lateral reinforcements were applied, and the effect of lateral reinforcement was also investigated. Finally, the influence of the lateral reinforcement on the lateral behavior of the 3D-printed columns was noted.

2. Mixture Proportions

Table 1 provides details on the composition of the mixture used for the 3D printing process, which comprised ordinary Portland cement (OPC) with a density of 3.14 g/cm^3, as well as two types of cementitious materials: silica fume (SF) and class C fly ash (FA). SF was used as a supplementary cementitious material and had a SiO_2 content of 91.3% to improve extrusion and bonding properties. The addition of SF to the concrete mixture provides better workability for the mixtures as well as good viscosity [25]. Moreover, class C FA has a specific gravity of 2.26 g/cm^3 and a loss on ignition of 2.8%. The use of FA in the mixture has a beneficial effect on improving the adhesiveness at the fresh stage of the concrete filament and the pozzolanic activity [26,27]. In addition, the presence of FA in the concrete mixture also reduces concrete shrinkage during the hardening process [28]. To ensure good extrusion during the printing process, sand with a grain size ranging from 0.16–0.2 mm was chosen. A high-performance water-reducing agent (HWRA) was also added to the mixture to increase concrete filament extrusion under a low water–binder ratio of 0.29. Furthermore, a viscosity agent was added to the filament mixture, which not only prevented the component from segregating but also controlled the drying shrinkage of the filament by reducing water evaporation [29,30].

Table 1. Mixing proportions of the concrete filaments.

W/B (%)	Unit Weight (kg/m^3)						
	Water	OPC	SF	FA	Sand	HWRA	Viscosity Agent
0.29	240	576	79	172	1154	8.27	1.65

3. Experimental Details

3.1. Experimental Process

An experimental flowchart is presented in Figure 2. The mixture was prepared as mentioned in the previous section. Then, column specimens were printed by the gantry system. Steel angles were applied to some column specimens (AN column series), and couplers were used for the other column specimens (CP column series) to connect the column specimens to the foundation. During the printing process, two types of lateral reinforcement with two different spacings were attached to the printed layers to improve the bonding and shear strength of the column.

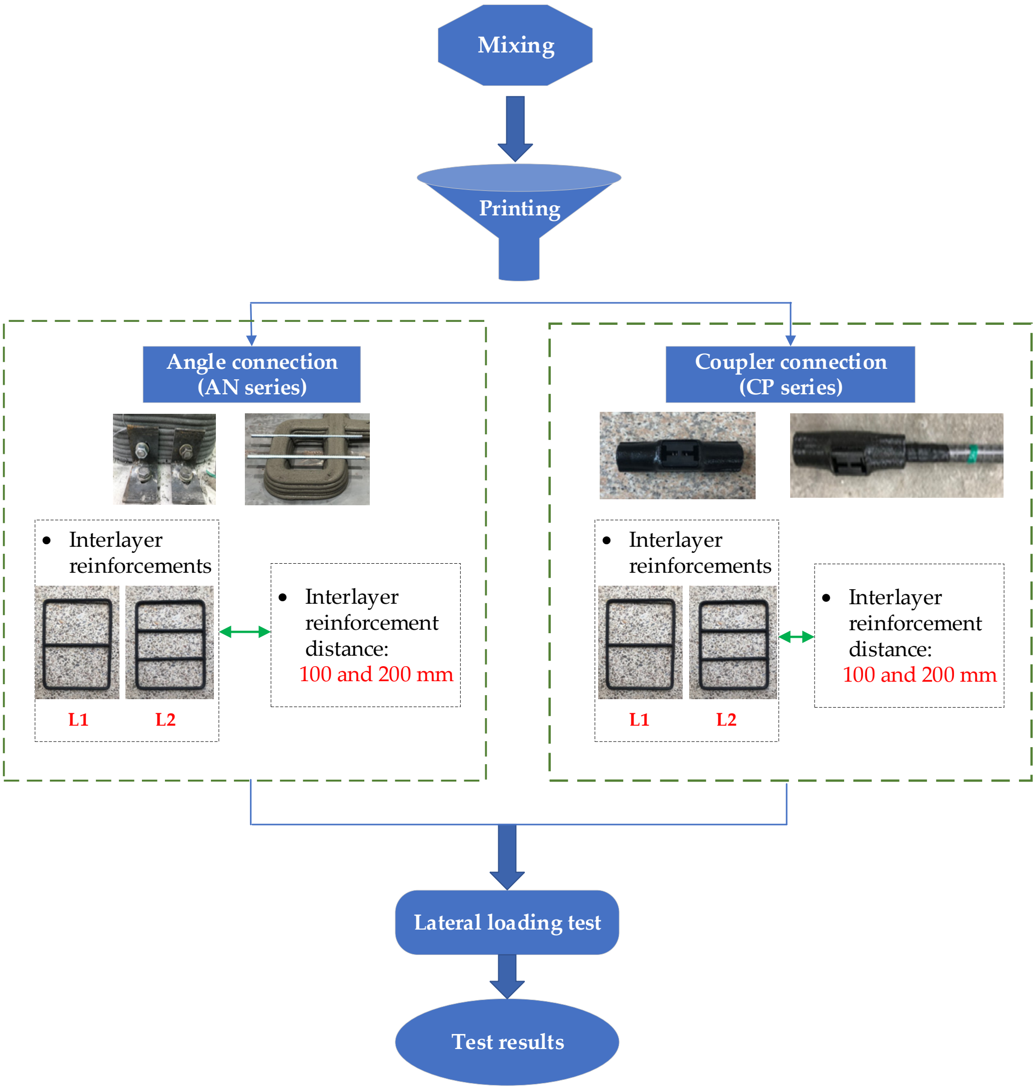

Figure 2. Experimental flowchart.

3.2. Connector and Lateral Reinforcement Types

Two types of connections between the printed structure and foundation were examined. For the column specimens with steel angle connections (called the AN connection type), the wall of the printed structure and the foundation were connected by steel angles and anchor bolts, as shown in Figure 2. Two walls of the printed structure were connected by connector bolts. For the column specimens with coupler connections (called the CP connection type), the printed structure and the foundation were connected by rebar incorporating the coupler.

To improve the bonding strength at the interlayer on the printed structure, two types of lateral reinforcements were installed at the interface of the printed layer during the printing process. The lateral reinforcements are shown in Figure 2. In the figure, the L1 and L2 letters identify each ladder rebar type shown. We expected that the application of the lateral reinforcements would improve the bonding strength and the shear resistance of the 3D-printed structure subjected to horizontal loading.

The printed columns and their detailed characteristics are listed in Table 2. All printed columns have a height of 1200 mm and cross dimensions of 200 × 250 mm, as shown in Figure 3. The printed layer has a bead width of 50 mm and a thickness of 10 mm. The AN and CP letters denote the connection type with steel angle systems and couplers, respectively. The letters H100 and H200 indicate lateral reinforcement spacings of 100 mm and 200 mm, respectively.

Table 2. Experimental parameters of specimens.

Column	Connector Type	Lateral Reinforcement Type	Spacing of Lateral Reinforcement (mm)	Number of Vertical Rebar
AN-L1-H100	AN	L1	100	4-D13
AN-L1-H200			200	4-D13
AN-L2-H100		L2	100	4-D13
AN-L2-H200			200	4-D13
CP-L1-H100	CP	L1	100	4-D13
CP-L1-H200			200	4-D13
CP-L2-H100		L2	100	4-D13
CP-L2-H200			200	4-D13

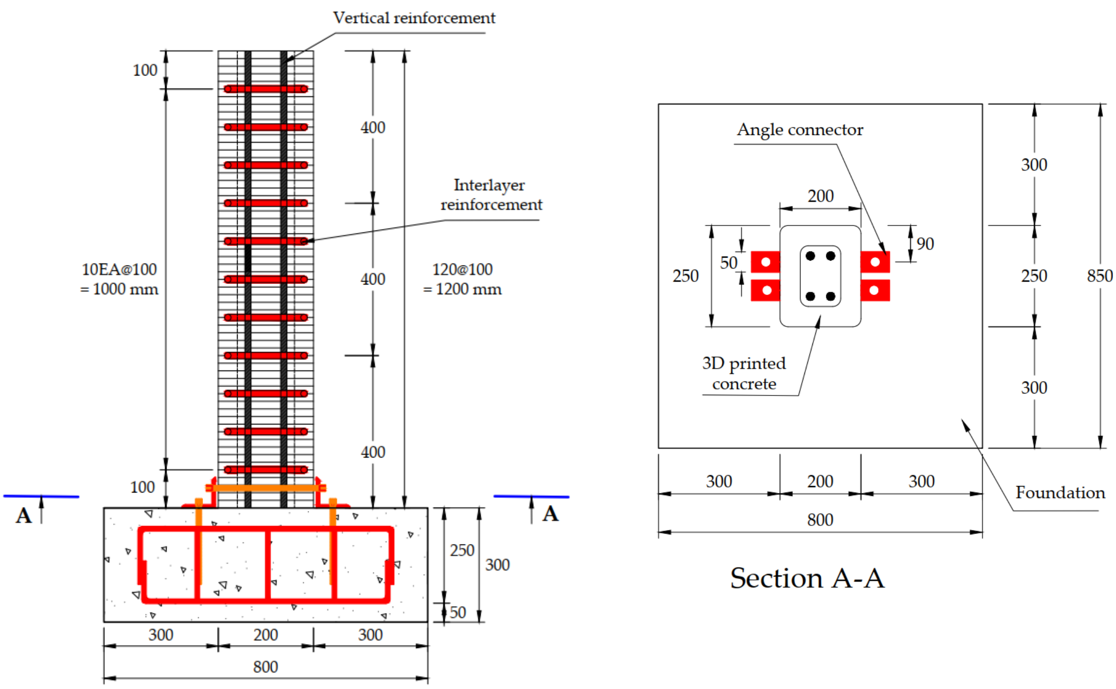

(a)

Figure 3. *Cont.*

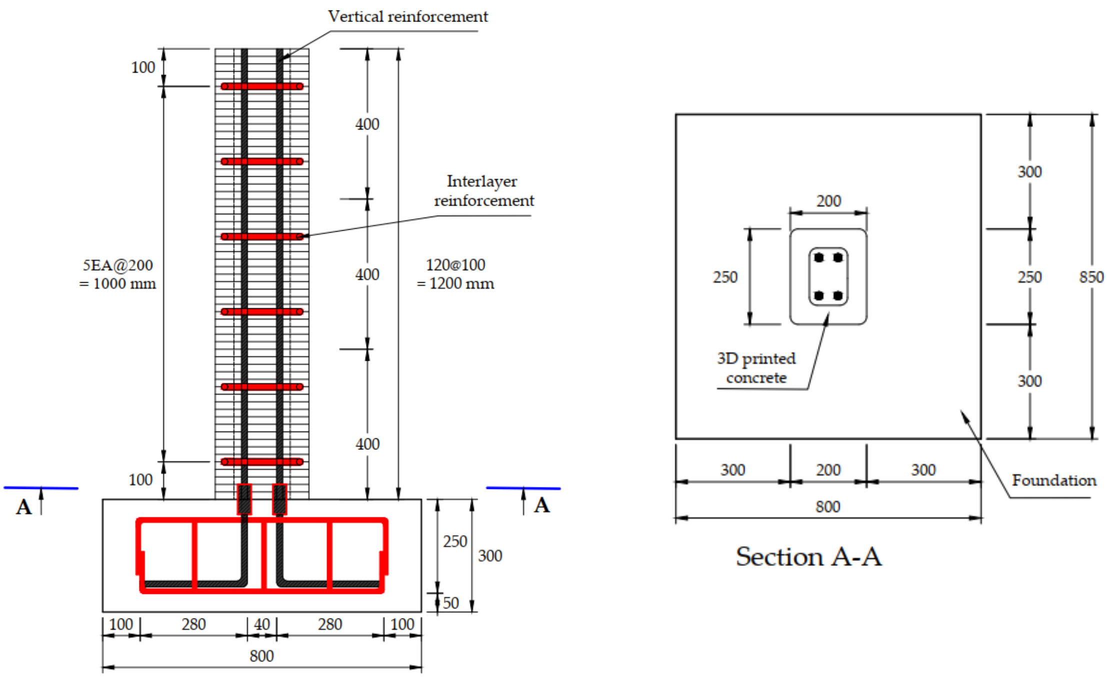

(**b**)

Figure 3. Details of a typical column series. (**a**) AN column series; (**b**) CP column series.

The details of the foundation are presented in Figure 4. The foundation has dimensions of 800 × 850 × 300 mm. The foundation was reinforced by grid rebar with a spacing of 150 mm.

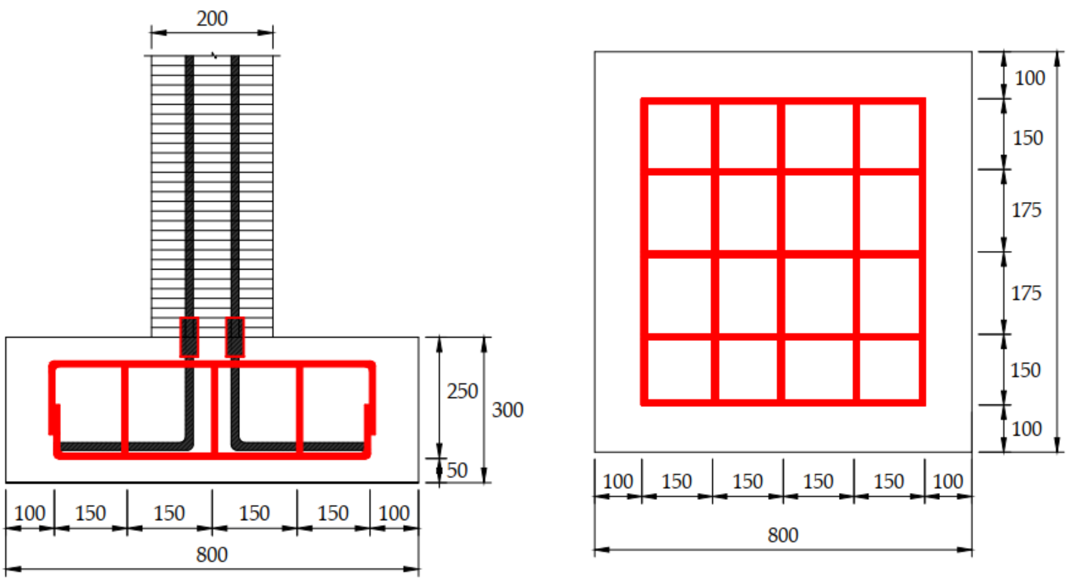

(**a**) (**b**)

Figure 4. Details of rebars in the foundation. (**a**) Elevation; (**b**) Top view.

3.3. Printing Process

Figure 5 depicts the printing gantry system, which is capable of moving along the X, Y, and Z axes. The printing procedure comprises three phases: data preparation, concrete filament preparation, and component printing. During the data preparation stage, a code file is generated to produce the printing path for each layer. In the concrete filament preparation phase, the mixture is prepared and deposited into a container. After the freshly mixed concrete is loaded into the container, it is smoothly conveyed through the pump–pipe–nozzle system to produce self-compacting concrete filaments. These filaments are used to create structural components layer by layer. The printing process, including controlling the nozzle height, printing speed, and printing direction, is managed by both the controller and the PC systems.

Figure 5. Gantry printing system.

The time scenario for the printing process is presented in Figure 6. There are two large structures (each structure includes four target structures) printed in this study. These two structures were printed alternately during the printing process. Per printing cycle, 40 layers of each structure were printed within 60 min. Therefore, the break time for each printing cycle was 60 min after 40 layers of the structures were printed. Figure 7 shows the printing process of the second structure after 40 layers of the first structure were printed.

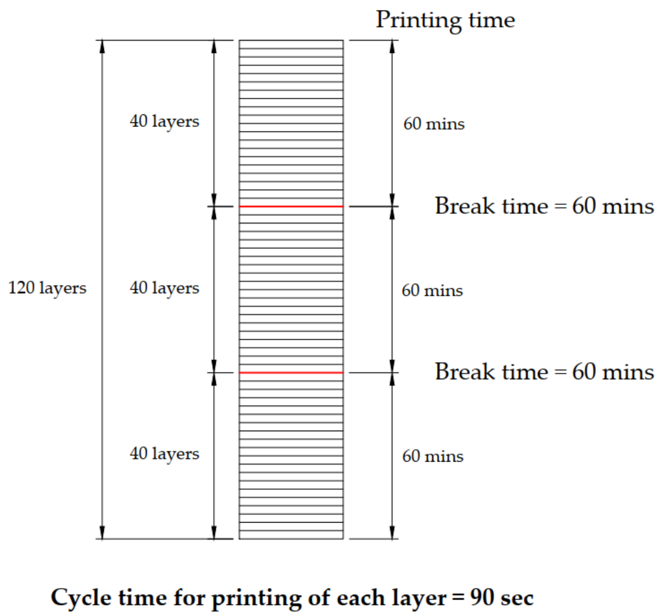

Figure 6. Time scenario for the printing process.

(**a**) (**b**)

Figure 7. Printing process for the columns. (**a**) Printing process; (**b**) After completing printing.

3.4. Connecting Method

For the AN column series, as shown in Figure 8, the foundation was fabricated with four holes for installing the screw bolts connecting the column and foundation. Then, the column was located at the positions of the bolt holes, and the bolts were screwed into the holes. Finally, four vertical rebars were located in the hollow of the column, and concrete was poured into this hole.

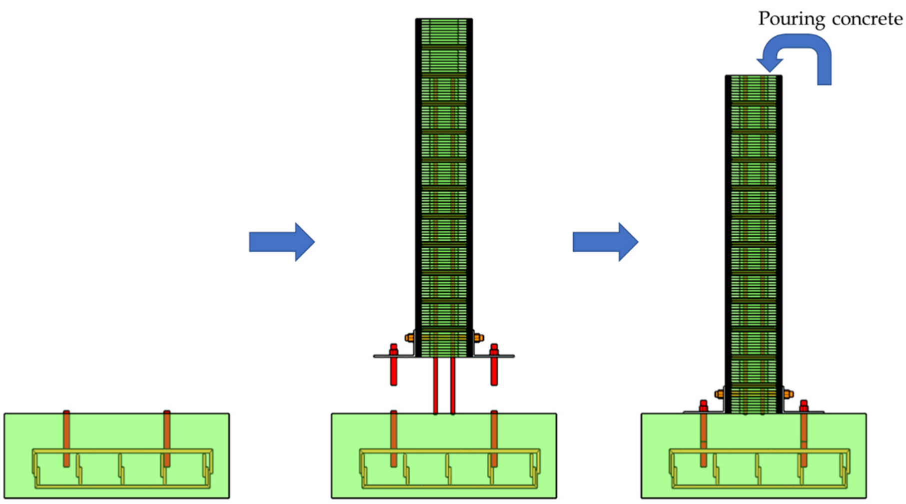

Figure 8. Connecting method for the AN column series.

For the CP column series, the fabrication process is shown in Figure 9. Four rebars with a bend of 90 degrees at the end of the rebar were located in the foundation. The opposite ends of these rebars were connected to the rebar in the column with couplers. Finally, the column was placed over the foundation, and concrete was poured into this hollow column.

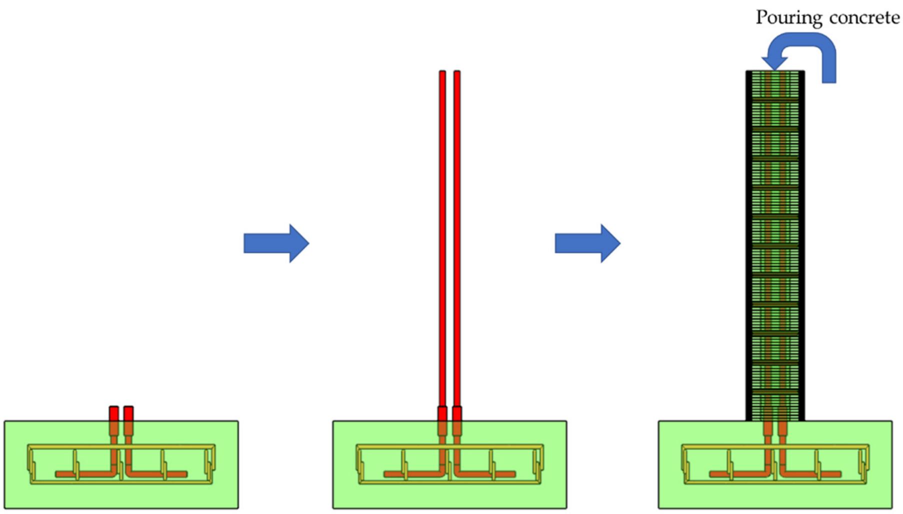

Figure 9. Connecting method for the CP column series.

3.5. Testing Method and Instruments

The test setup for the printed structures is provided in Figure 10. A horizontal load was applied to the printed structures near the top of the structure at a distance of 100 mm. To obtain the displacement of the tested structure, three linear variable differential transformers (LVDTs) were placed horizontally on the side face of the structures. One wire LVDT was placed at the top of the structure, and the other was placed at the middle at a distance of 600 mm from the top. The third LVDT was set close to the footing at a distance of 200 mm. An illustration of the lateral loading test is shown in Figure 10b. Four high-strength ground anchors were used to fix the column onto the strong floor of the laboratory, with the loading stub being subjected to lateral loading. The lateral test as implemented is shown in Figure 11.

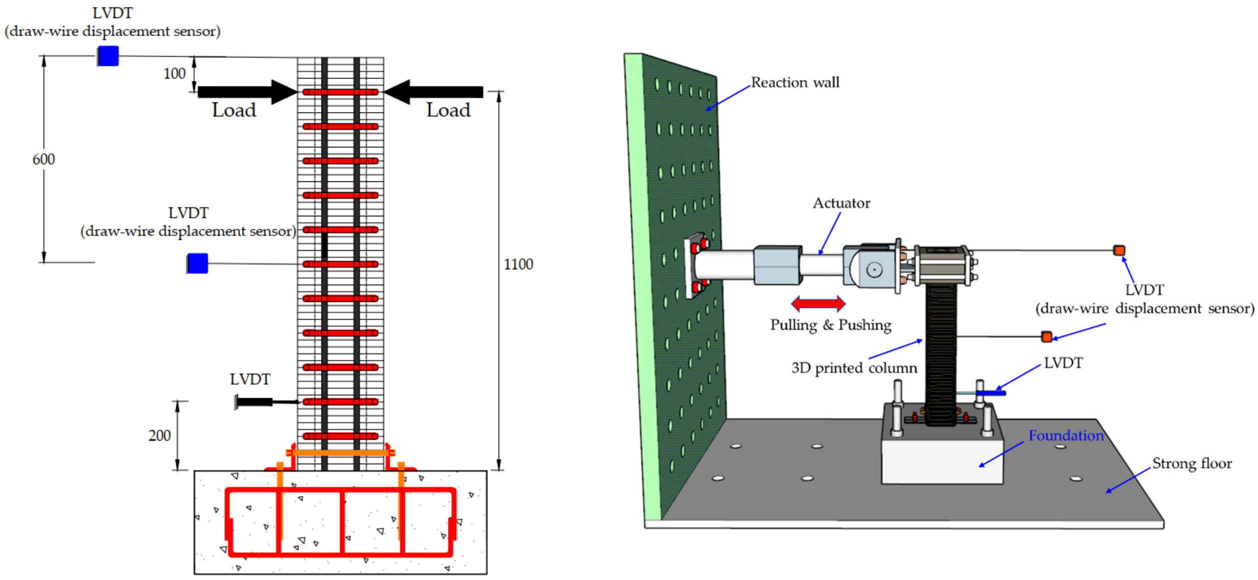

(**a**) (**b**)

Figure 10. Lateral loading test method. (**a**) Test set up for 3D-printed structures; (**b**) illustration of the lateral loading test.

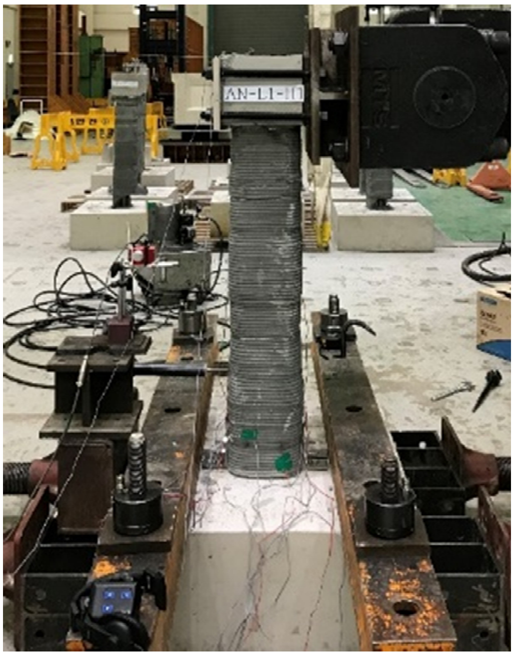

Figure 11. Actual lateral loading test.

The cycling load of the lateral loading test is shown in Table 3 and Figure 12. Three drift ratios of 3.64%, 7.73%, and 10.91% were studied, which corresponded to displacements of 40, 80, and 120 mm, respectively. For each drift ratio, one load cycle was performed.

Table 3. Drift ratio.

Drift Ratio (%)	Displacement (mm)	Cycle Number
3.64	40	1
7.73	80	1
10.91	120	1

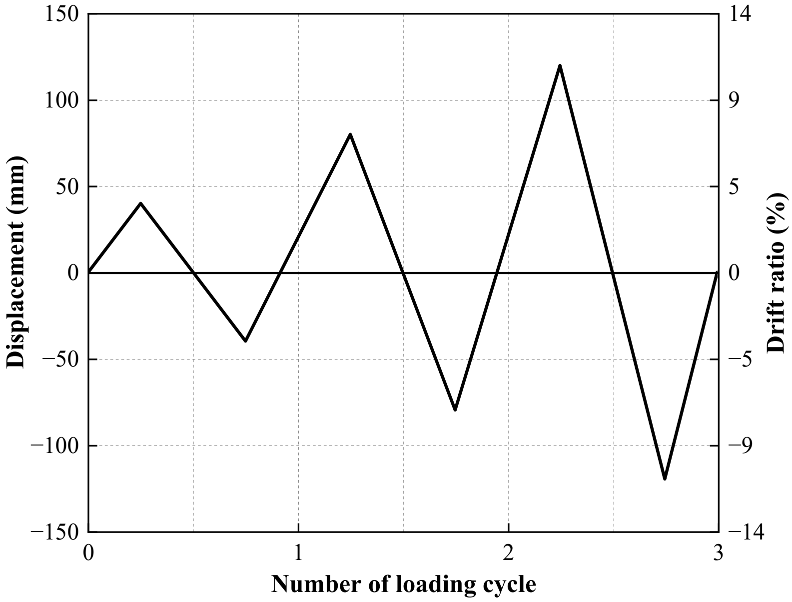

Figure 12. Cycling load.

4. Test Results and Discussion

4.1. Typical Failure Pattern

The deformed shapes of the AN-L1-H200 structure under pushing and pulling at each displacement are shown in Figure 13. The initial cracks occurred at the 5th layer from the bottom in the northern face of the structure at a displacement of 40 mm. This crack propagated down to the second layer of the east face. Then, it propagated up to the fifth layer of the southern face of the structure at further displacements. It ultimately widened and became the major crack at the failure stage.

Displacement	**Specimens**	
(mm)	**AN column series (AN-L1-H200)**	**CP column series (CP-L1-H200)**
Initial stage	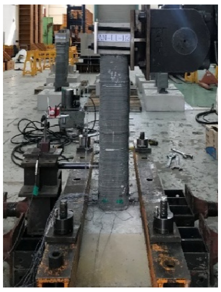	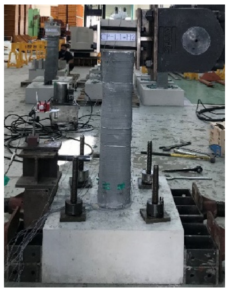
40	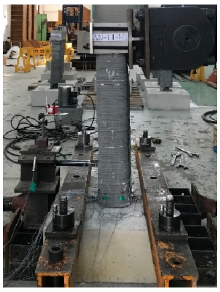	
80	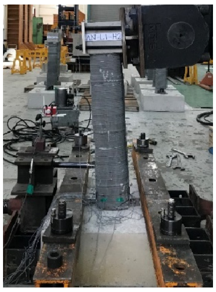	
120	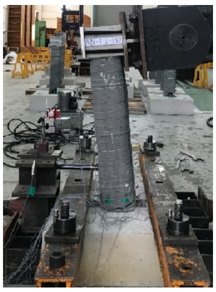	

Figure 13. Deformed shapes.

The deformed shapes of the CP-L1-H200 structure under pushing and pulling at each displacement are shown in Figure 13. The initial cracks occurred at the bottom first layer in the east face of the structure at a displacement of 40 mm. Then, this crack propagated up to two sides of the east face. It was clearly visible that these cracks occurred due to the separation between the printed layers and the filling concrete. With further displacement, several layers of the printed concrete spalled off at the southern face. This failure pattern of the CP-L1-H200 column was different from that of the AN-L1-H200 column. For the AN-L1-H200 column, the filling concrete and the printed layer were connected by horizontal connecting bolds; thus, debonding between the filling concrete and the printed layers was not observed in this series. The filling concrete and printed layers should be connected by horizontal reinforcements to reduce the risk of debonding failure.

The typical failure pattern and cracking localization of the AN column specimen are shown in Figure 14. This failure reveals that the failure of the printed structure was accompanied by separation at the position of the connecting bolts (layer 5th). These cracks propagated from the southern face to the western face of the printed structure.

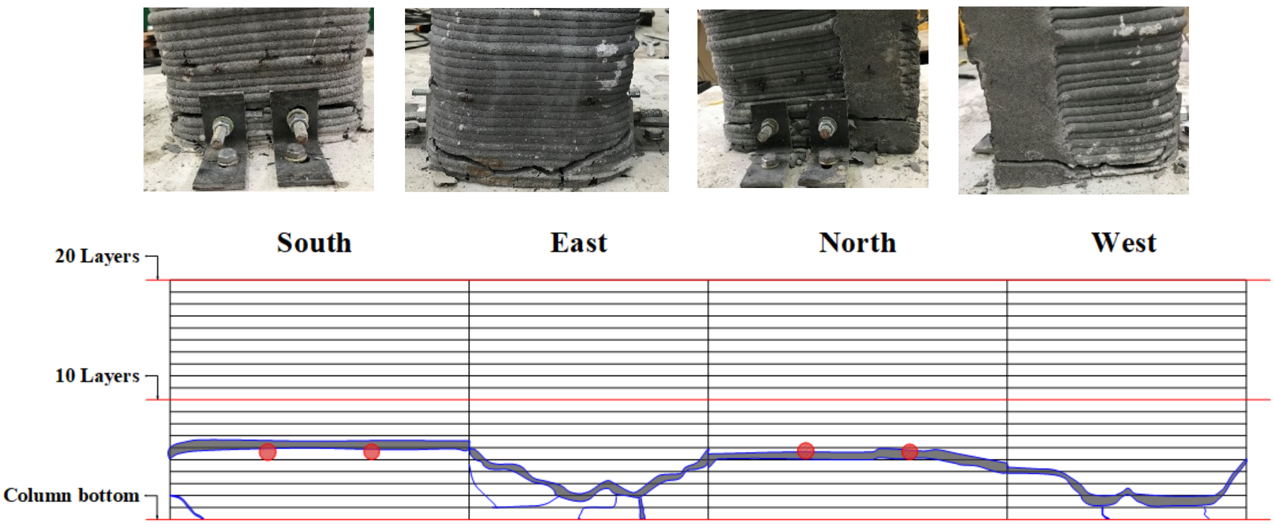

Figure 14. Typical crack mapping of AN column series.

The failure pattern and cracking localization of the CP column specimen are shown in Figure 15. This pattern reveals that the failure of the printed structure occurred by the separation of the printed layer and the filling concrete, as shown in the east face. Some spalling parts were observed in the south, north and west faces of the structure. The spalling part was clearly observed in the south and north faces. As mentioned in the above discussion, the debonding between the filling concrete and the printed layers could be prevented by the horizontal connecting bolts in the AN column series. Therefore, it is assumed that the debonding between the filling concrete and the printed layers in the CP column series might be prevented by adding more lateral reinforcements at the lower position of the column.

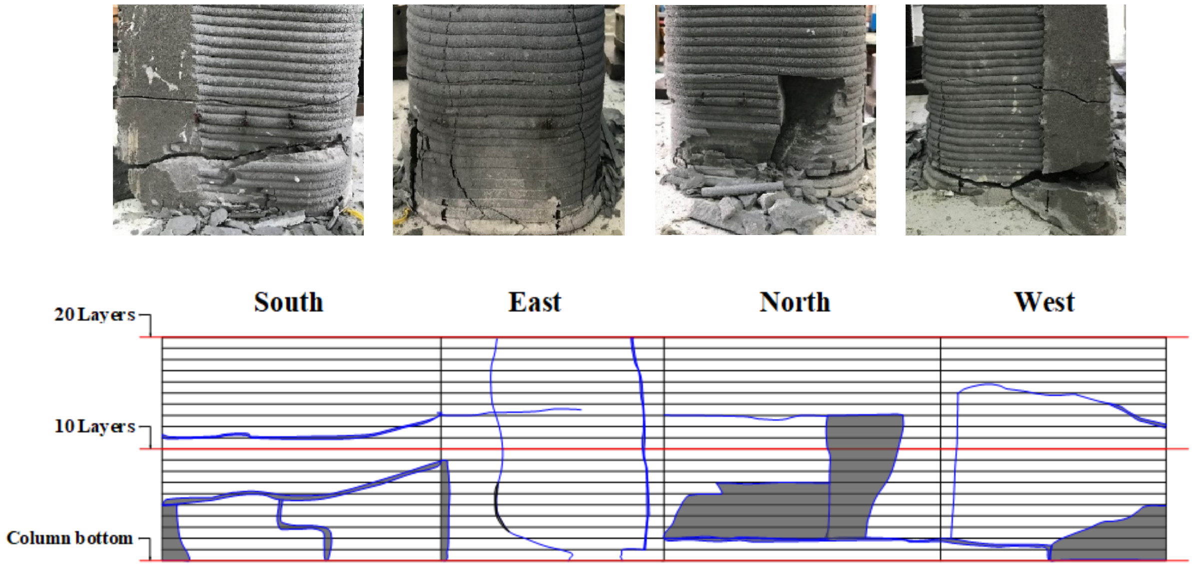

Figure 15. Typical crack mapping of CP column series.

4.2. Lateral Response

4.2.1. The Effect of Connector Types

The main test results of the columns under lateral loading are shown in Table 4. Figure 16 shows the typical lateral response of the AN column and CP column series. The residual drift ratio was calculated as the ratio of residual displacement to the shear span of the column of 1100 mm. The AN-L1-H100 column achieved a peak load of 5.04 kN in the first loading cycle at a residual drift ratio of 2.1%. Then, the load capacity of the column tended to decrease. When the drift ratio reached 3.64%, the load of the column was 4.15 kN. For the second loading cycle, the load of the column was reduced. The peak load for the second loading cycle was 3.25 kN when the column achieved a residual drift ratio of 5.66%. At a drift ratio of 7.27%, the load of the column was 3.09 kN. For the third loading cycle, the peak load of the column was 2.50 kN, corresponding to a residual drift ratio of 11.08%. At a drift ratio of 10.91%, the load of the column was 2.47 kN.

For the CP-L1-H100 column, the load capacity of the column reached a value of 7.5 kN when the drift ratio was 3.64%. Then, the load of the column continued to increase up to a peak load of 8.13 kN at a residual drift ratio of 3.85%. For the second loading cycle, the load of the column was 11.64 kN when the column reached a residual drift ratio of 7.27%. At the third loading cycle, the load capacity of the CP-L1-H100 column tended to decrease slightly. At a drift ratio of 10.91%, the load of the column was 10.8 kN, and then it increased to a peak load of 11.26 kN with a drift ratio of 11.34%.

The load-displacement envelope curves of the AN and CP column series at various positions of columns are shown in Figure 16b. The load-displacement envelope curves were obtained by connecting the peak points in the hysteresis curve at each cycle. For the AN-L1-H100 column, the column reached the maximum load at the first loading cycle. This result indicates that the reduction in load after reaching the maximum load resulted from the deformation of the steel angles and the slippage of the column during loading. The column was connected to the foundation by steel angles; thus, the core rebar could not add strength to the column during the test.

In contrast to the AN-L1-H100 specimen, this column absorbed an increasing load at further drift ratio levels. The CP-L1-H100 column achieved the peak load at the second drift ratio levels, and the load was slightly reduced at the last loading cycle. This phenomenon is attributed to the connection between the column and the foundation. The core rebars of the column were connected to the foundation through couplers, so the core rebar could carry the lateral load during the test. This contribution directly improved the strength of the column; thus, the load of the column tended to increase at further drift ratio levels.

Table 4. Lateral performance indices of test specimens.

Column Specimen	1st Loading Cycle (θ = 3.64%)				2nd Loading Cycle (θ = 7.27%)				3rd Loading Cycle (θ = 10.91%)				Failure Mode
	$P_{peak,1}$ (kN)	$\Delta_{peak,1}$ (mm)	θ_r (%)	E_1 (kN.mm)	$P_{peak,2}$ (kN)	$\Delta_{peak,2}$ (mm)	θ_r (%)	E_2 (kN.mm)	$P_{peak,3}$ (kN)	$\Delta_{peak,3}$ (mm)	θ_r (%)	E_3 (kN.mm)	
AN-L1-H100	5.04	24.6	2.24	276.36	3.25	45.4	4.13	444.47	2.50	121.9	11.08	567.23	Debonding at connecting bolt
AN-L1-H200	4.54	18.8	1.71	235.10	2.41	34.6	3.15	404.59	1.51	129.7	11.79	595.49	Debonding at connecting bolt
AN-L2-H100	4.63	34.1	3.10	308.63	3.93	46.7	4.25	453.45	2.49	127.4	11.58	594.92	Debonding at connecting bolt
AN-L2-H200	4.14	14.3	1.30	274.86	2.77	49.3	4.48	417.86	2.21	128.8	11.71	610.87	Debonding at connecting bolt
CP-L1-H100	8.13	42.4	3.85	465.44	11.90	84.8	7.71	1054.72	11.26	124.8	11.35	1562.55	Concrete debonding
CP-L1-H200	6.99	43.3	3.94	223.11	9.09	72.9	6.63	914.61	7.12	127.4	11.58	1595.43	Concrete debonding
CP-L2-H100	6.25	43.5	3.95	377.78	9.89	86.1	7.83	956.62	10.49	128.3	11.66	1543.65	Concrete debonding
CP-L2-H200	11.00	36.1	3.28	515.39	11.29	84.6	7.69	1016.99	12.21	124.0	11.27	1388.74	Concrete debonding

Note: P: Lateral load; θ: drift ratio; θ_r: residual drift ratio; Δ: displacement at different lateral loads; E: dissipated energy.

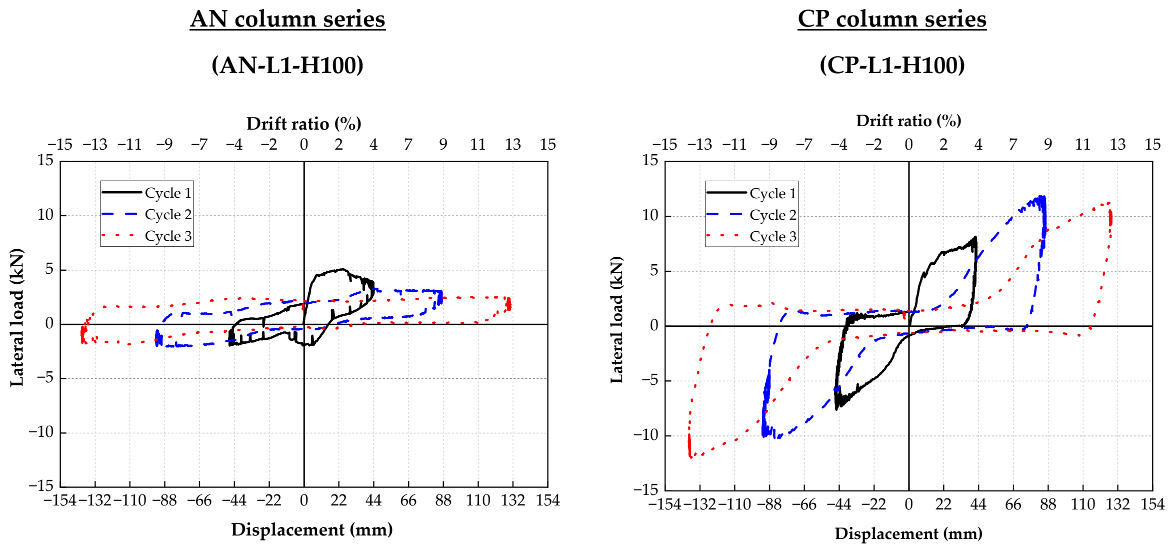

(**a**)

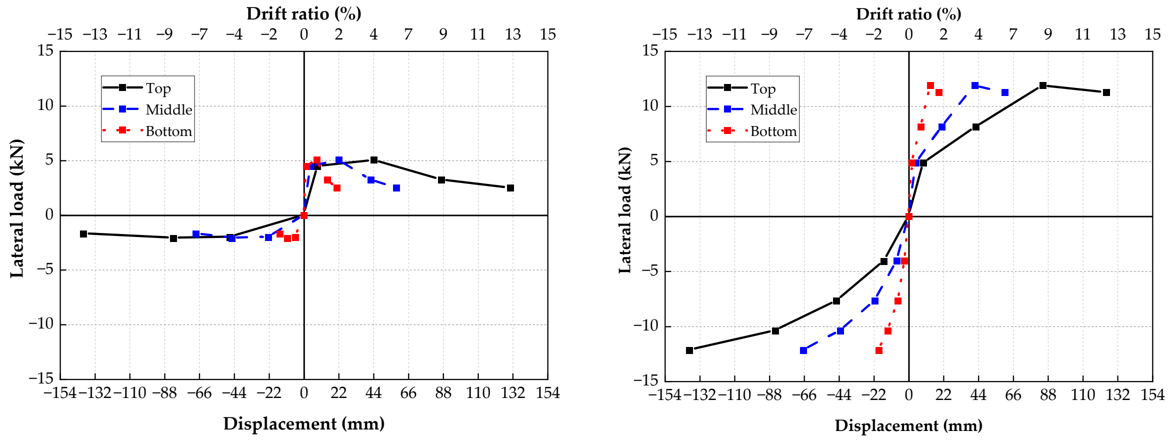

(**b**)

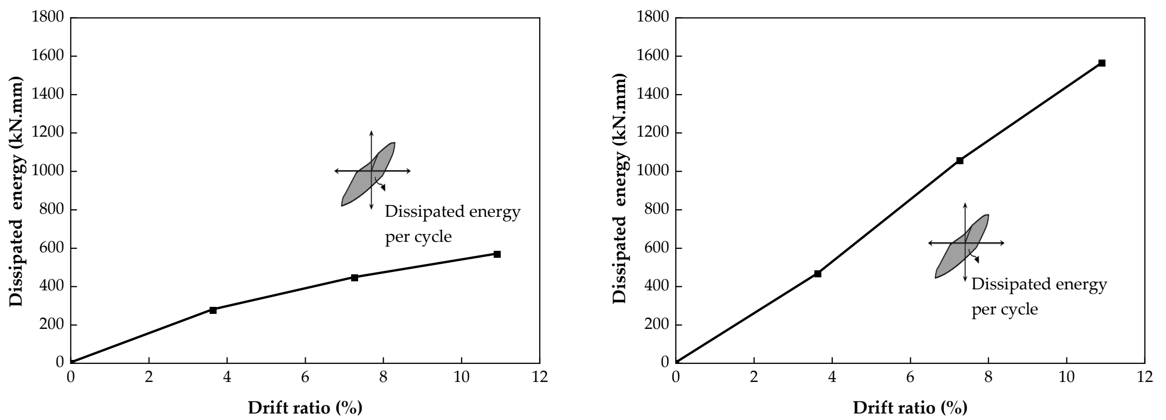

(**c**)

Figure 16. Typical lateral responses of AN and CP column series. (**a**) Hysteresis curve; (**b**) Load-displacement envelope curves; (**c**) Residual drift ratio curves.

The dissipated energy at different drift ratios of the column is presented in Figure 16c. The energy dissipation capacity, which represents the ability of a structural component to consume lateral loading energy via plastic deformation under lateral loading, was determined. The amount of energy dissipated per cycle of loading was calculated by measuring the area enclosed by the hysteresis loop at a designated displacement level. This shows that the dissipated energy of the AN-L1-H100 and CP-L1-H100 columns tended to increase at further drift ratios. The dissipated energies of the AN-L1-H100 column at drift ratios of 3.64%, 7.27%, and 10.91% were 276.36 kN-mm, 444.47 kN-mm, and 567.23 kN-mm, respectively. Meanwhile, higher values of dissipated energy were obtained in the CP-L1-H100 column. The dissipated energies of the CP-L1-H100 column at drift ratios of 3.64%, 7.27%, and 10.91% were 465.44 kN-mm, 1054.72 kN-mm, and 1562.55 kN-mm, respectively.

A comparison of the dissipated energy between the column with a steel angle and the column with a coupler is shown in Figure 17. As shown, the columns with the coupler connection type had a superior load capacity to that of the columns with the steel angle connection type. The load capacities of the CP-L1-H100 and CP-L2-H200 columns were approximately four times greater than that of the AN column series. This comparison indicates that the use of a coupler for the connection between the column and foundation significantly improved the load capacity of the column under lateral loading. As shown, the load of the CP column series tended to increase after the first loading cycle. Meanwhile, the AN column series showed a slightly decreasing load tendency after reaching the peak load at the first loading cycle. This result suggested that the core rebars of the CP columns contributed to the strength of these column series. Because the core rebars of these column series were connected to the foundation by the couplers, these rebars could handle the lateral load during testing and improve the overall strength of the columns. However, for the AN column series, core rebars were not connected to the foundation, so these rebars could not provide additional strength to the column. In addition, the AN column series was easily displaced because of column slippage and deformation of the steel angles. Therefore, a lower strength capacity was obtained in the AN column series.

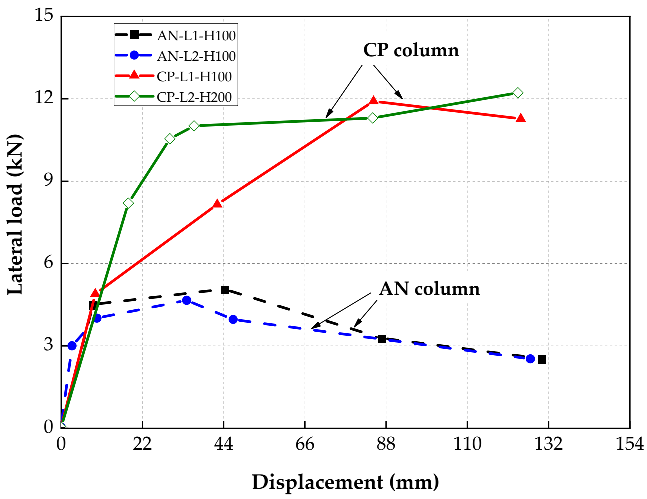

Figure 17. Comparison of the lateral load-displacement curves of the columns with different connection types.

A comparison of the dissipated energy of the two-column series at various drift ratios is shown in Figure 18. At the first drift ratio of 3.64%, the cumulative dissipated energies of the two-column series were quite similar. The CP column series exhibited relatively larger dissipated energy when compared to the other column series. For the AN column series, the cumulative dissipated energies of the AN-L1-H100, AN-L1-H200, AN-L2-H100, and AN-L2-H200 columns were 276.36, 235.10, 308.63, and 274.86 kN-mm, respectively. The CP column series showed higher dissipated energies of 465.44, 223.11, 377.78, and 515.39 kN mm for the CP-L1-H100, CP-L1-H200, CP-L2-H100, and CP-L2-H200 columns, respectively.

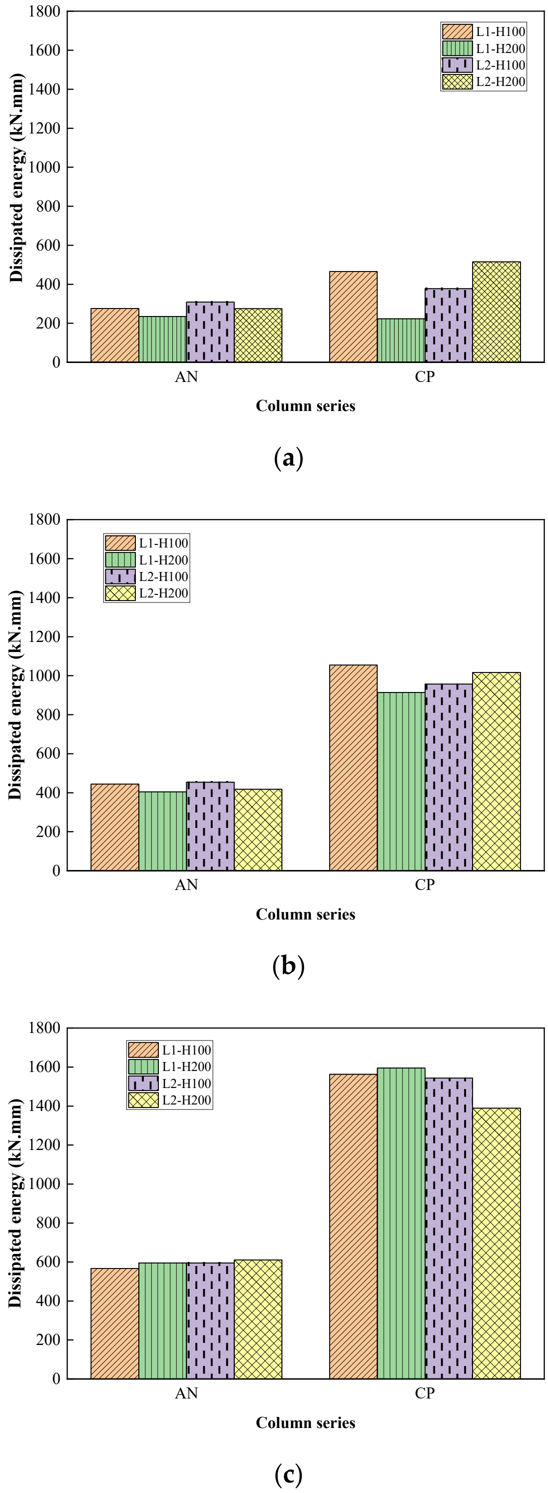

Figure 18. Comparison of dissipated energy between AN and CP column series at various drift ratios. (**a**) Dissipated energy at a drift ratio of 3.64%; (**b**) dissipated energy at a drift ratio of 7.27%; (**c**) dissipated energy at a drift ratio of 10.91%.

At the second drift ratio of 7.27%, the CP column series showed a higher cumulative dissipated energy than the AN column series. The test results showed that the dissipated energy of the CP column series was approximately two times greater than that of the AN column series. The dissipated energy of the AN column series was approximately

400 kN-mm. Meanwhile, the CP column series exhibited dissipated energy in the range of 900~1050 kN-mm.

At the last drift ratio of 10.91%, although an increasing amount of dissipated energy was observed in the AN column series, this dissipation was not significant. The dissipated energy from the AN column series increased by approximately 20% at the last drift ratio. Meanwhile, a more significant amount of dissipated energy was obtained in the CP column series. For the CP column series, the dissipated energy increased approximately 1.5 times at the last loading cycle. The data indicate that the core rebars in the CP column series were well connected to the foundation; thus, the core rebars carried the lateral load during the test. Therefore, a large amount of dissipated energy was absorbed in the two-column series. Simultaneously, the AN columns were connected to the foundation by the steel angles; thus, the columns could slip, and the steel angles were deformed under the lateral load. Therefore, less dissipated energy was absorbed in this column series.

4.2.2. The Effect of Lateral Reinforcement Types

A comparison of the load-displacement curves between the columns with L1 and L2 reinforcement is shown in Figure 19. As shown in Figure 19a, for the columns with a lateral distance of 100 mm, the load capacity of the AN-L2-H100 column was insignificantly higher than that of the AN-L1-H100 column. Additionally, the load capacity of the CP-L1-H100 column was greater than that of the CP-L2-H100 column. For the H200 column series, the AN-L1-H200 column exhibited a greater load capacity than the AN-L2-H200 column.

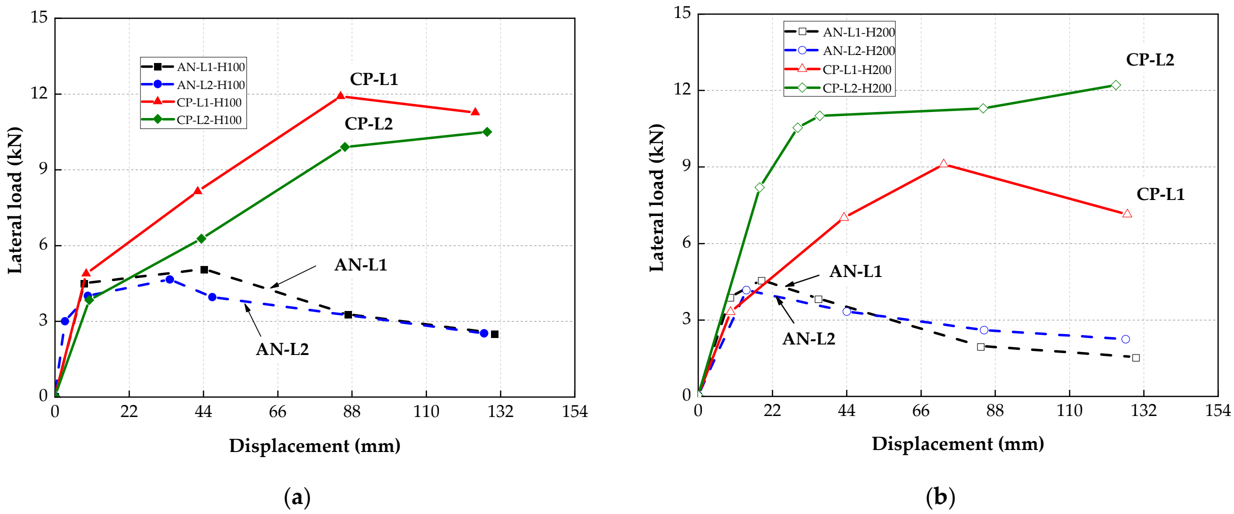

Figure 19. Comparison of load-displacement curves. (**a**) Spacing = 100 mm (H100 series); (**b**) Spacing = 200 mm (H200 series).

For the H200 column series, the AN-L1-H200 and AN-L2-H200 columns had similar load capacities. In contrast to the H100 series, the load capacity of the CP-L2-H200 column was significantly greater than that of the CP-L1-H200 column, as shown in Figure 19b. Moreover, the load capacity of the CP-ST-H200 was significantly higher than that of the AN-L1-H200, AN-L2-H200, and CP-L1-H200 columns. Based on these results, a clear tendency indicating an influence of the lateral reinforcement types was not observed. This lack of influence might have been observed because the use of lateral reinforcement improved the buildability of the printing process; thus, the contribution of the lateral reinforcement to the strength of the 3D-printed column was not significant. In addition, the early fracture of the columns occurred at the connection position, leading to the failure of the column. Hence, the effects of the lateral reinforcement on the lateral loading behavior of the column were not clear.

Figure 20 describes the effect of lateral reinforcement types on the drift ratio of the 3D-printed column. For the columns with a lateral reinforcement spacing of 100 mm, the drift ratio curves of the AN-L1-H100 and AN-L2-H100 columns were quite similar. Meanwhile, a clear tendency in the drift ratio curve of the CP-L1-H100 and CP-L2-H100 columns was not observed. At a drift ratio of 3.64%, the residual drift ratio of the CP-L2-H100 column was less than that of the CP-L1-H100 column. However, at further drift ratio levels, higher residual drift ratios were obtained in the CP-L2-H100 column.

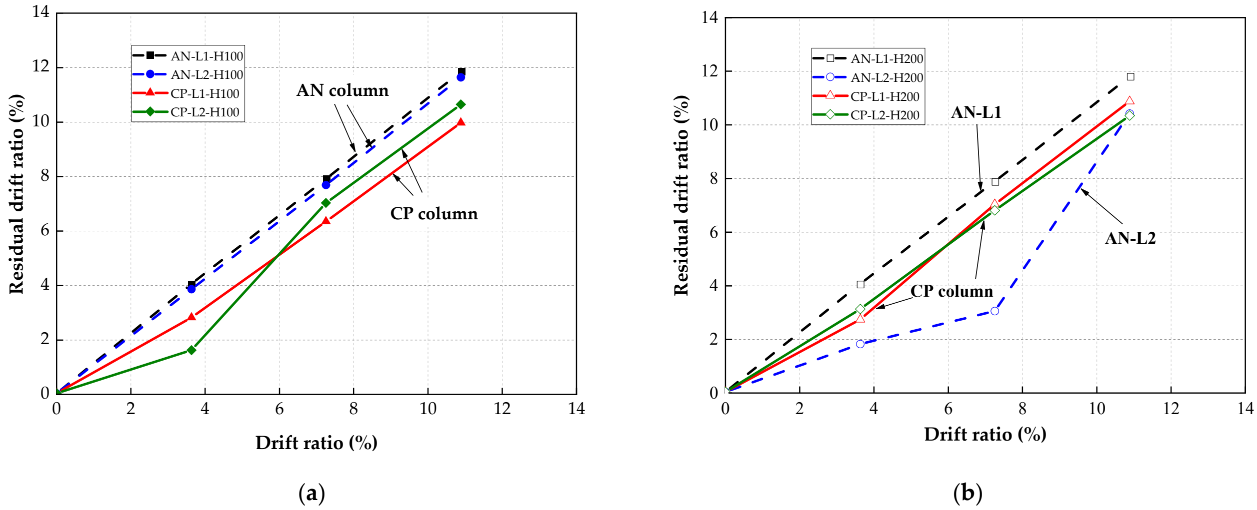

Figure 20. Comparison of drift ratio curves. (**a**) H100 series; (**b**) H200 series.

For the H200 column series, the drift ratio curve of the AN-L2-H200 column was less than that of the AN-L1-H200 column and showed the lowest value of the residual drift ratio. In addition, the drift ratio curves of the CP-L1-H200 and CP-L2-H200 columns were quite similar. We consider that the lateral reinforcement types did not clearly affect the residual drift ratio of the 3D-printed columns.

4.2.3. The Effect of Lateral Reinforcement Distance

The effect of the lateral reinforcement distance on the load-displacement behavior of the 3D-printed column is shown in Figure 21. For the AN column series, the column with a shorter lateral reinforcement distance exhibited a higher load capacity than the column with a longer lateral reinforcement distance. The load capacity of the AN-L1-H100 column was 11.01% greater than that of the AN-L1-H200 column. In addition, the load capacity of the AN-L2-H100 column was 11.84% greater than that of the AN-L2-H200 column.

For the CP column series, an inverted tendency of the load-displacement behavior of the 3D-printed column was observed. The column with the longer lateral reinforcement distance showed a greater load capacity than the column with the shorter lateral reinforcement distance. The CP-L2-H200 column had a higher load capacity than the CP-L2-H100 column. The peak load of the CP-L2-H200 column was 12.21 kN, while that of the CP-L2-H100 column was 10.49 kN. The CP-L1-H100 column with a shorter lateral reinforcement distance exhibited a superior loading capacity when compared to that of the CP-L1-H200 column. These results indicate that a clear effect of the lateral reinforcement distance was not obtained. This result indicated that lateral reinforcement improved the buildability of the printing process, which increased the interlayer strength of the printed layers. Therefore, the distance of the lateral reinforcement insignificantly affected the lateral loading behavior of the 3D-printed column.

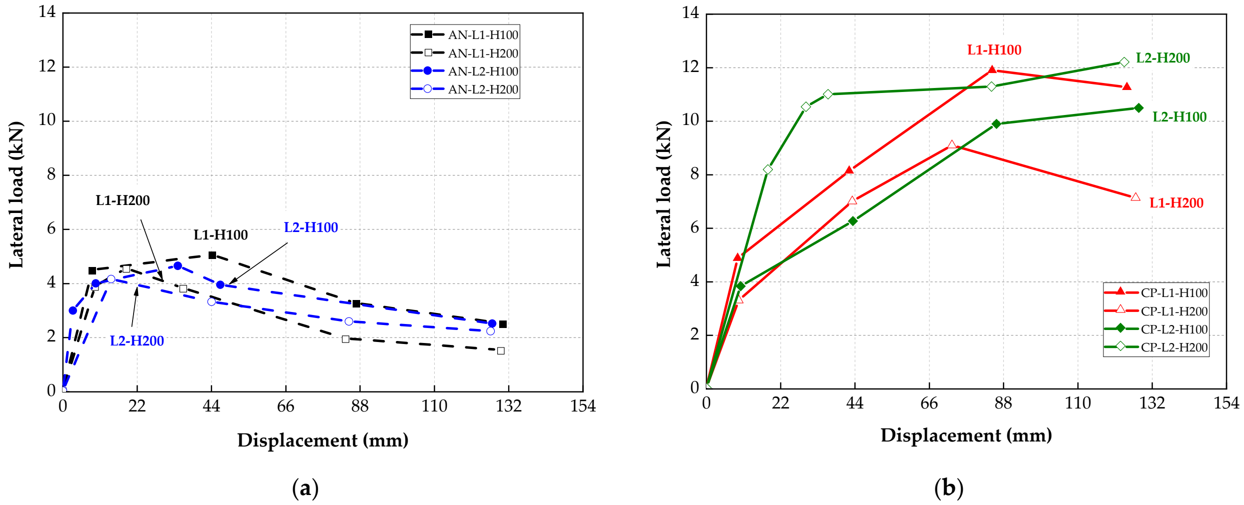

Figure 21. Comparison of the load-displacement at various lateral reinforcement distances. (**a**) Steel angle connection (AN series); (**b**) Coupler connection (CP series).

Figure 22 shows the influence of the lateral reinforcement distance on the residual drift ratio of the 3D-printed column. For the AN column series, the drift ratio curves of the AN-L1-H100 and AN-L1-H200 columns were similar at various drift ratio levels. The drift ratio curves of the AN-L1-H100 and AN-L1-H200 columns at a drift ratio of 10.91% were 11.85% and 11.79%, respectively. Meanwhile, the drift ratio curve of the AN-L2-H200 column was less than that of the AN-L2-H100 column at the various drift ratio levels. At a drift ratio of 10.91%, the residual drift ratio of the AN-L2-H200 column was 11.82% less than that of the AN-L2-H100 column.

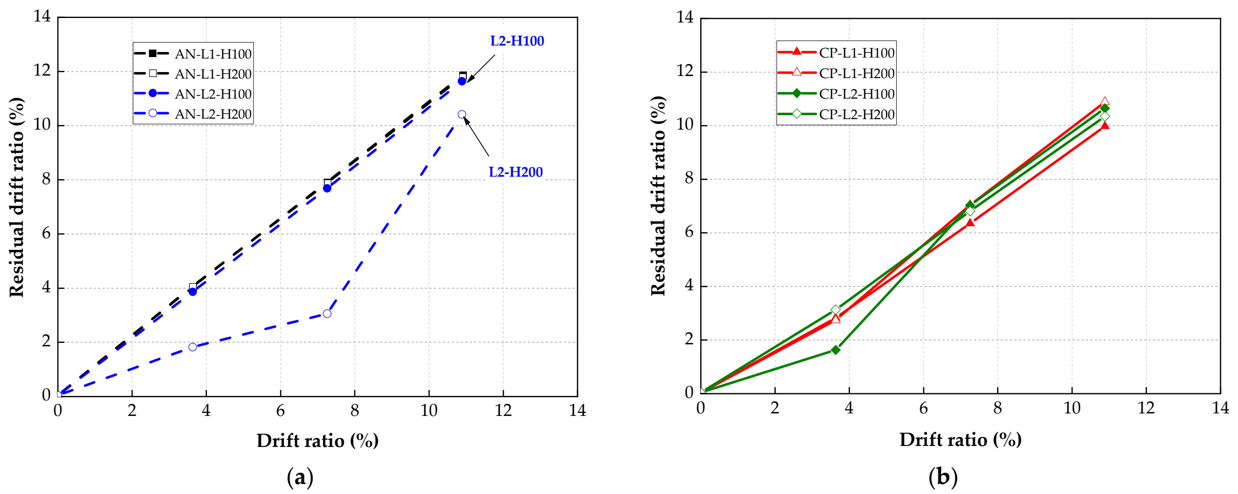

Figure 22. Comparison of the drift ratio at various lateral reinforcement distances. (**a**) AN series; (**b**) CP series.

For the CP column series, the residual drift ratio curves were quite similar to each other. The residual drift ratios of the CP-L1-H100, CP-L1-H200, CP-L2-H100, and CP-L2-H200 columns at a drift ratio of 10.91% were 9.96%, 10.87%, 10.64%, and 10.34%, respectively. Therefore, it can be concluded that the lateral reinforcement spacing did not affect the residual drift ratio of the 3D-printed columns.

5. Conclusions

This study investigates the lateral behavior of 3D-printed columns. More specifically, the effects of the following connector types were investigated: steel angle and coupler, lateral reinforcement types, and lateral reinforcement spacing. Based on our results, the main conclusions are provided as follows:

1. In terms of load capacity, the column specimens with coupler connections exhibited superior load capacity when compared to that of column specimens with angle connections. The load capacity of the CP column series was approximately four times greater than that of the AN column series. This result indicated that the AN column series slipped, and the steel angles were deformed during the test, resulting in a lower load capacity. Moreover, the CP column series with the couplers connecting the core rebar and foundation allowed the rebar to carry the lateral load during the test.
2. The test results revealed that the CP column series exhibited a lower residual drift ratio than the AN column series. This phenomenon indicates that the use of a coupler for the connection is more advanced against the displacement of the column.
3. Although two types of lateral reinforcements were used to improve the bonding strength of the printed layer and shear resistance, the influence of lateral reinforcement in the two series was not obvious. Similarly, the effect of the lateral reinforcement distance on the lateral behavior of the two series was insignificant.
4. The test results showed that the dissipated energy of the columns with couplers was two times greater than that of the columns with steel angles. This result indicates that the core rebar could contribute its strength to the lateral loading strength of the column by using couplers.

Author Contributions: Conceptualization, I.-H.Y. and Q.-T.B.; Data curation, S.-T.J.; Formal analysis, Q.-T.B.; Investigation, J.-H.P.; Resources, S.-T.J.; Software, Q.-T.B.; Supervision, I.-H.Y.; Visualization, Q.-T.B.; Writing—original draft preparation, Q.-T.B.; Writing—review and editing, I.-H.Y. All authors have read and agreed to the published version of the manuscript.

Funding: This work was supported by the Human Resources Development of the Korea Institute of Energy Technology Evaluation and Planning (KETEP) grant funded by the Korean government Ministry of Trade, Industry and Energy (No. 20214000000180).

Data Availability Statement: The data used to support the findings in this study are available from the corresponding author upon request.

Conflicts of Interest: The authors declare that they have no conflict of interest regarding the publication of this manuscript.

References

1. Siddika, A.; Al Mamun, M.A.; Ferdous, W.; Saha, A.K.; Alyousef, R. 3D-Printed Concrete: Applications, Performance, and Challenges. *J. Sustain. Cem. Based Mater.* **2020**, *9*, 127–164. [CrossRef]
2. Lyu, F.; Zhao, D.; Hou, X.; Sun, L.; Zhang, Q. Overview of the Development of 3D-Printing Concrete: A Review. *Appl. Sci.* **2021**, *11*, 9822. [CrossRef]
3. Zhang, J.; Wang, J.; Dong, S.; Yu, X.; Han, B. A Review of the Current Progress and Application of 3D Printed Concrete. *Compos. Part A Appl. Sci. Manuf.* **2019**, *125*, 105533. [CrossRef]
4. Sanjayan, J.G.; Nematollahi, B. Chapter 1-3D Concrete Printing for Construction Applications. In *3D Concrete Printing Technology*; Sanjayan, J.G., Nazari, A., Nematollahi, B., Eds.; Butterworth-Heinemann: Oxford, UK, 2019; pp. 1–11, ISBN 978-0-12-815481-6.
5. Apis-Cor. Available online: https://www.apis-cor.com (accessed on 15 March 2022).
6. Scott, C. Chinese Construction Company 3D Prints an Entire Two-Story House On-Site in 45 Days. Available online: https://3dprint.com/138664/huashang-tengda-3d-print-house/ (accessed on 15 March 2022).
7. Salet, T.A.M.; Ahmed, Z.Y.; Bos, F.P.; Laagland, H.L.M. Design of a 3D Printed Concrete Bridge by Testing. *Virtual Phys. Prototyp.* **2018**, *13*, 222–236. [CrossRef]
8. Kreiger, E.L.; Kreiger, M.A.; Case, M.P. Development of the Construction Processes for Reinforced Additively Constructed Concrete. *Addit. Manuf.* **2019**, *28*, 39–49. [CrossRef]
9. Shanghai Opens World's Longest 3D-Printed Concrete Bridge. Available online: https://edition.cnn.com/style/article/shanghai-3d-printed-bridge-scli-intl/index.html (accessed on 15 March 2022).
10. Jones, K.E.S.; Li, M. Life Cycle Assessment of Ultra-Tall Wind Turbine Towers Comparing Concrete Additive Manufacturing to Conventional Manufacturing. *J. Clean Prod.* **2023**, *417*, 137709. [CrossRef]
11. Tall Wind Turbine Towers with 3D-Printed Concrete Bases. Available online: https://www.bft-international.com/en/artikel/bft_Tall_wind_turbine_towers_with_3D-printed_concrete_bases-3555202.html (accessed on 15 March 2022).

12. Marchment, T.; Sanjayan, J. Mesh Reinforcing Method for 3D Concrete Printing. *Autom. Constr.* **2020**, *109*, 102992. [CrossRef]
13. Cohen, Z.; Carlson, N. Piling and Pressing: Towards a Method of 3D Printing Reinforced Concrete Columns. *Constr. Robot.* **2020**, *4*, 61–73. [CrossRef]
14. Joh, C.; Lee, J.; Bui, T.Q.; Park, J.; Yang, I.-H. Buildability and Mechanical Properties of 3D Printed Concrete. *Materials* **2020**, *13*, 4919. [CrossRef]
15. Ahmed, G.H.; Askandar, N.H.; Jumaa, G.B. A Review of Largescale 3DCP: Material Characteristics, Mix Design, Printing Process, and Reinforcement Strategies. *Structures* **2022**, *43*, 508–532. [CrossRef]
16. Marchment, T.; Sanjayan, J.G.; Nematollahi, B.; Xia, M. Interlayer Strength of 3D Printed Concrete: Influencing Factors and Method of Enhancing. In *3D Concrete Printing Technology*; Elsevier: Amsterdam, The Netherlands, 2019; pp. 241–264.
17. Zareiyan, B.; Khoshnevis, B. Effects of Interlocking on Interlayer Adhesion and Strength of Structures in 3D Printing of Concrete. *Autom. Constr.* **2017**, *83*, 212–221. [CrossRef]
18. Babafemi, A.J.; Kolawole, J.T.; Miah, M.J.; Paul, S.C.; Panda, B. A Concise Review on Interlayer Bond Strength in 3D Concrete Printing. *Sustainability* **2021**, *13*, 7137. [CrossRef]
19. Hass, L.; Bos, F. Bending and Pull-Out Tests on a Novel Screw Type Reinforcement for Extrusion-Based 3D Printed Concrete. In *Second RILEM International Conference on Concrete and Digital Fabrication*; Springer: Berlin/Heidelberg, Germany, 2020; pp. 632–645, ISBN 978-3-030-49915-0.
20. Park, J.; Bui, Q.-T.; Lee, J.; Joh, C.; Yang, I.-H. Interlayer Strength of 3D-Printed Mortar Reinforced by Postinstalled Reinforcement. *Materials* **2021**, *14*, 6630. [CrossRef] [PubMed]
21. Ma, G.; Li, Z.; Wang, L.; Bai, G. Micro-Cable Reinforced Geopolymer Composite for Extrusion-Based 3D Printing. *Mater. Lett.* **2019**, *235*, 144–147. [CrossRef]
22. Bester, F.; van den Heever, M.; Kruger, J.; Cho, S.; van Zijl, G. Steel Fiber Links in 3D Printed Concrete. In *Second RILEM International Conference on Concrete and Digital Fabrication*; Springer: Berlin/Heidelberg, Germany, 2020; pp. 398–406, ISBN 978-3-030-49915-0.
23. Perrot, A.; Jacquet, Y.; Rangeard, D.; Courteille, E.; Sonebi, M. Nailing of Layers: A Promising Way to Reinforce Concrete 3D Printing Structures. *Materials* **2020**, *13*, 1518. [CrossRef]
24. Bos, F.P.; Ahmed, Z.Y.; Wolfs, R.J.M.; Salet, T.A.M. *3D Printing Concrete with Reinforcement BT—High Tech Concrete: Where Technology and Engineering Meet*; Hordijk, D.A., Luković, M., Eds.; Springer International Publishing: Cham, Switzerland, 2018; pp. 2484–2493.
25. Pacewicz, K.; Sobotka, A.; Gołek, Ł. Characteristic of Materials for the 3D Printed Building Constructions by Additive Printing. *MATEC Web Conf.* **2018**, *222*, 01013. [CrossRef]
26. Zhang, Y.; Zhang, Y.; Liu, G.; Yang, Y.; Wu, M.; Pang, B. Fresh Properties of a Novel 3D Printing Concrete Ink. *Constr. Build Mater.* **2018**, *174*, 263–271. [CrossRef]
27. Li, Y.; Kwan, A.K.H. Ternary Blending of Cement with Fly Ash Microsphere and Condensed Silica Fume to Improve the Performance of Mortar. *Cem. Concr. Compos.* **2014**, *49*, 26–35. [CrossRef]
28. Tran, N.P.; Gunasekara, C.; Law, D.W.; Houshyar, S.; Setunge, S.; Cwirzen, A. A Critical Review on Drying Shrinkage Mitigation Strategies in Cement-Based Materials. *J. Build. Eng.* **2021**, *38*, 102210. [CrossRef]
29. Cappellari, M.; Daubresse, A.; Chaouche, M. Influence of Organic Thickening Admixtures on the Rheological Properties of Mortars: Relationship with Water-Retention. *Constr. Build. Mater.* **2013**, *38*, 950–961. [CrossRef]
30. Khayat, K.H. Viscosity-Enhancing Admixtures for Cement-Based Materials—An Overview. *Cem. Concr. Compos.* **1998**, *20*, 171–188. [CrossRef]